2021 43rd Annual International Conference of the
IEEE Engineering in Medicine & Biology Society (EMBC)
Oct 31 - Nov 4, 2021. Virtual Conference

L_1–L_2 Minimization Via A Proximal Operator For Fluorescence Molecular Tomography

Heng Zhang[1,2], Hongbo Guo[1,2], Shuangchen Li[1,2], Yanqiu Liu[1,2], Xuelei He[1,2], Xiaowei He[1,2,*] and Yuqing Hou[1,2,*]

Abstract— Fluorescent Molecular Tomography (FMT) is a highly sensitive and noninvasive imaging method that provides three-dimensional distribution of biomarkers by noninvasive detection of fluorescent marker probes. However, due to the light scattering effect and ill-posedness of inverse problems, it is challenging to develop an efficient construction method that can provide the exact location and morphology of the fluorescence distribution. In this paper, we proposed $L_1 - L_2$ norm regularization to improve FMT reconstruction. In our research, proximal operators of non-convex $L_1 - L_2$ norm and forward-backward splitting method was adopted to solve the inverse problem of FMT. Simulation results on heterogeneous mouse model demonstrated that the proposed FBS method is superior to IVTCG, DCA and IRW-$L_{1/2}$ reconstruction methods in location accuracy and other aspects.

I. INTRODUCTION

With the development of medical imaging technology, the use of non-targeted or targeted exogenous fluorescent markers in clinical applications and biological research has increased exponentially [1] [2] [3]. As an extension of fluorescence imaging technology, fluorescence molecular tomography (FMT) can accurately visualize and quantify the three-dimensional (3D) distribution of fluorescence targets in deep turbidities by capturing the surface fluorescence distribution of fluorescence targets using an ultra-sensitive charge-coupled device (CCD) camera [4] [5].

However, due to the light scattering effect the inverse problem of the FMT is highly ill-posedness. In the past few years, in order to overcome this problem, many methods have been proposed in the reconstruction [6] [7]. One effective strategy is utilizing the spatial distribution of different biological tissues, which can be segmented from computed tomography (CT) and magnetic resonance imaging (MRI), as a prior information to construct the photon propagation model. In addition, proper regularization has always been an important method to alleviate the ill-posedness problem in FMT reconstruction [8] [9] [10]. Among the traditional methods, the Tikhonov regularization method is a typical method to solve ill-posedness problems, which adds the L_2 norm constraint to the original objective function. There are many standard minimum methods for solving L_2 norm regularization optimization problems, including Newtons method, conjugate gradient method and so all. But the over-smoothing of the L_2 norm results in blurred or diffused targets and it is difficult to obtain the sharp boundaries in the reconstructed results.

Because of the early tumors are always small and sparse in size compared to the entire body of the subject. Therefore, the accumulated fluorescent probes in tumors are also small and sparse, and it is reasonable to assume that the fluorescent signals are sparse [11]. According to compressed sensing theory, if a signal is sparse, it can be reconstructed from very few measurements. Mathematically, L_0 norm regularization is the sparsest constraint but infeasible for applications. So, some researchers choose L_1 norm regularization to obtain the distribution of the fluorescent probes [12] [13]. Various methods based on L_1 norm regularization have been proposed, such as the iterated shrinkage method with the L_1 norm (IS-L1) , interior-point method, fast iterative soft-thresholding algorithm (FISTA) , the incomplete variables truncated conjugate gradient algorithm (IVTCG) [14]; L_1 norm regularization method based on the Split Bregman method (SB-L1) , and gradient-based techniques. Beside that, some researchers have proposed a variety of solving methods based on $L_{1/2}$ norm to solve the inverse problem of FMT, such as IRW-$L_{1/2}$ [8] HTAP [15]. In recent years, the more excellent sparsity of $L_1 - L_2$ norm has attracted the attention of researchers, and put forward the corresponding solution method, namely DCA [16]. Compared with L_1 norm and $L_{1/2}$ norm regularization, $L_1 - L_2$ norm is sparser and performs better in the case of reconstruction small fluorescence probes [16].

In this paper, we adopted $L_1 - L_2$ norm regularization to resolve the inverse problem of FMT. To solve the nonconvex optimization problem which aroused by $L_1 - L_2$ norm regularization, we derived the proximal operators of $L_1 - L_2$ norm and used the framework of FBS method. To validated the performance of the proposed method in FMT reconstruction, we carried out single source and double sources simulation experiments and compared with DCA, IVTCG, IRW- method at the same time.

*This research is supported by the National Natural Science Foundation of China, Grant/Award Numbers:(61971350, 11871321, 61901374, 61906154, 82071914); Postdoctoral Innovative Talents Support Program, Grant/Award Number: (BX20180254); Project funded by China Post-doctoral Science Foundation, Grant/Award Number: (2018M643719); Science and Technology Plan Program in Xi'an of China, Grant/Award Number: (201805060ZD11CG44);

1 is with the Xi'an Key Laboratory of Radiomics and Intelligent Perception, Xi'an, China.

2 is with the School of Information Sciences and Technology, Northwest University, Xi'an, 710127, China.

∗ is corresponding author (houyuqin@nwu.edu.cn),(hexw@nwu.edu.cn).

II. Method

A. Photon propagation model

In biological bodies, photon propagation within the near-infrared spectral band has a highly scattering feature. For steady-state FMT with point excitation sources, the following coupled diffusion equations (DE) have been commonly used to model the forward problem of FMT [5]:

$$\begin{cases} \nabla \cdot (D_x(r)\nabla\Phi_x(r) - \mu_{ax}\Phi_x(r)) = -\Theta_s\delta(r - r_l) \\ \nabla \cdot (D_m(r)\nabla\Phi_m(r) - \mu_{am}\Phi_m(r)) = -\Phi_x(r)\eta\mu_{af}(r) \\ r \in \Omega \end{cases} \tag{1}$$

Where subscripts x and m denote the excitation and emission light respectively. Φ_x stands for the photon flux density, $D_{x,m}$ denote the diffusion coefficient in biological tissues, $D_{x,m} = 1/3[\mu_{ax,am} + (1-g)\mu_{sx,sm}]$, where $\mu_{ax,am}$ and $\mu_{sx,sm}$ represent the absorption coefficient and scattering coefficient respectively, g is the anisotropy parameter. $\eta\mu_{af}(r)$ represents the unknown fluorescence yield distribution to be reconstructed. $\Theta_s\delta(r-r_l)$ denotes the excitation light which is considered as the point source. r_l represents the position of a point source with an amplitude of Θ_s. $\delta(r)$ is the Dirac function.

We solve the diffusion equations combined with the Robin-type boundary condition by applying the adaptive finite element method, we can obtain a linear model:

$$\mathrm{A}x = \Phi \tag{2}$$

Where A is $M \times N$ vector which contains the boundary measurements, and x is an $N \times 1$ vector denotes the unknown internal distribution of the probes, Φ is an $M \times 1$ vector represents the measurements of surface photon distribution.

B. Reconstruction Based on the forward–backward splitting (FBS) Method

In this section, we proposed a practical FBS method, which used to solve FMT inverse problem. Since only the photon distribution on the surface can be measured, the dimension of the measurement is much smaller than the dimension of the internal fluorescence distribution, leading to the, ill-posedness of the FMT problem. As we all know, a proper norm regularization often used to overcome the ill-posedness of the FMT problem. $L_1 - L_2$ norm has been shown to overcome ill-posedness. Considering the advantage of $L_1 - L_2$ norm regularization, we write (2) as (3).

$$\tfrac{1}{2}||\mathrm{A}x - \Phi||_2^2 + \lambda(||x||_1 - ||x||_2) \tag{3}$$

Where λ is the regulation parameter. We decompose (3) into $F(x) = f(x) + g(x)$, where

$$\begin{aligned} f(x) &= \tfrac{1}{2}||\mathrm{A}x - \Phi||_2^2 \\ \mathrm{g}(x) &= \lambda(||x||_1 - ||x||_2) \end{aligned} \tag{4}$$

Use forward–backward splitting (FBS) method to resolve minimization problem (3) can get the following results:

$$\begin{aligned} x^k &\in prox_\rho(g)(x_g) \\ &= \arg\min_x \lambda\left(||x||_1 - ||x||_2\right) + \tfrac{1}{2\rho}||x - x_g||_2^2 \\ &= \arg\min_x ||x||_1 - ||x||_2 + \tfrac{1}{2\sigma}||x - x_g||_2^2 \end{aligned} \tag{5}$$

where $x_g = x^k - \mathrm{A}'(\mathrm{A}x - \Phi)$,

Proximal operator is particularly useful in convex optimization. For example, the proximal operator L_1 for is called soft shrinkage, which defined as:

$$s_1(y,t) = \begin{cases} y - t, & if \quad y > t \\ 0, & if \quad |y| \le t \\ y + t, & if \quad y < -t \end{cases} \tag{6}$$

We define x^* as the optimal solution of the optimization problem (3), it can straightforward to obtain the following relations:

$$\begin{aligned} &x_i^* \ge 0, \quad if \quad x_{g_i} > 0 \\ &x_i^* \le 0, \quad if \quad x_{g_i} < 0 \\ &|x_i^*| > |x_j^*| \quad if \quad |x_{g_i}| > |x_{g_j}| \end{aligned} \tag{7}$$

Because in FMT, the non-negative constraint on the unknown vector ($x_{g_i} \ge 0, \quad x_i \ge 0$), we can assume without loss of generality is a non-negative non-increasing vector, $x_{g_1} \ge x_{g_2} \ge \cdots x_{g_N} \ge 0$, and help us circumvent any complications due to the non-differentiability of the L_1 norm penalty near zero.

Appoint $G(x) = ||x||_1 - ||x||_2 + \frac{1}{2\sigma}||x - x_g||_2^2$, and its first-order of $G(x)$ is:

$$G'(x) = \begin{cases} (1 - \dfrac{\sigma}{||x||_2})x - x_g - \sigma q & for \quad x \ne 0 \\ ||x_g - \sigma q||_2 - \sigma & for \quad x = 0 \end{cases} \tag{8}$$

Where $q \in \partial||x||_1$ is a subgradient of the L_1 norm. By the above statement, we can give the optimal solution x^* to the optimization problem in (5):

1) When $x_{g_1} > \sigma$, $x^* = z(||z||_2 + \sigma)/||z||_2$, where $z = s_1(x_g, \sigma)$;

2) When $x_{g_1} \le \sigma$, x^* is an optimal solution if and only if it is a 1-sparse vector. For x^*, $x_i^* = x_{g_1}$, else $x_i^* = 0$;

The flowchart of the main steps of FBS method is given in table 1.

TABLE I
Algorithm of The FBS method

Input: A, Φ, $x^1 = 0$
For $k = 1$ to K do
$x_g = x^k - \rho\mathrm{A}'(x - \Phi)$
$x^{k+1} = prox_\rho(g)(x_g)$
$x^k = x^{k+1}$
End for

III. EXPERIMENTS AND RESULTS

In this section, the simulations on 3D digital mouse model will used to evaluate the feasibility of the FBS algorithm for FMT reconstruction. To further quantify the property of FBS, the location error (LE), dice coefficient (Dice), signal-to-noise ratio (CNR) were employed in this study.

LE was defined as the location error of the reconstruction area and the real fluorescent area as follows:

$$LE = ||L_r - L_0||_2 \tag{9}$$

Where L_r is the center of the reconstructed area and L_0 is the barycenter of the real fluorescent area.

Dice was introduced to evaluate the similarity of the reconstruction area and the real fluorescent area:

$$Dice = \frac{2|s_r \cap s_0|}{|s_r| + |s_0|} \tag{10}$$

Where s_r is the reconstruction area, and s_0 is the fluorescent area.

CNR was performed to demonstrate the contrast of the reconstructed signal and background:

$$CNR = \frac{\mu_{ROI} - \mu_{ROB}}{\sqrt{\omega_{ROI}\sigma_{ROI}^2 + \omega_{ROB}\sigma_{ROB}^2}} \tag{11}$$

Where ω_{ROI} is the weight coefficient of the region of interest (ROI) and ω_{ROB} is the weight coefficient of the region of back-ground (ROB). μ_{ROI}, σ_{ROI} are the mean values and standard deviations of ROI and μ_{ROB}, σ_{ROB} are the mean values and standard deviations of ROB respectively.

The all experiment codes were written in MATLAB and were performed on a desktop computer with 2.90 GHz Intel Processor I5-9400F and 16G RAM.

In the numerical simulations, A 33mm height torso extracted from a 3D mouse atlas was utilized to simulate the heterogeneity of biological tissues [17]. which consisted of six organs, i.e., muscle, heart, liver, stomach, kidneys and lungs. Figure 1(a) shows the mouse model with six organs. Which consist of muscle, heart, liver, stomach, kidneys and lungs. Table 2 lists the related optical properties [18], and the excited light wave length is 650nm, the emission wavelength is 670nm. Single fluorescent source and dual fluorescent sources were set in the stomach, respectively in figure 1(b) and figure 1(c), which to prove the practicality and feasibility of FBS in FMT reconstruction; In both single-target and double-target experiments, a sphere with a radius of 2mm was used to simulate the fluorescence target, and two point sources used in this experiment, their positions are shown in the two circles in Figure 1(d), which were located one transport mean free path beneath the surface on the plane of Z = 17.5mm.

TABLE II
Optical parameters for the mouse organs

Material	μ_{ax}	μ'_{sx}	μ_{am}	μ'_{sm}
Muscle	0.0052	1.08	0.0068	1.03
Heart	0.0083	1.01	0.0104	0.99
Lungs	0.0133	1.97	0.0203	1.95
Liver	0.0329	0.70	0.0176	0.65
Kidneys	0.0660	2.25	0.0380	2.20
Kidneys	0.0660	2.25	0.0380	2.20
Stomach	0.0114	1.74	0.0070	1.36

In the whole process of the experiment, we used four contrast methods, including the proposed FBS, difference of convex algorithm (DCA), the incomplete variables truncated conjugate gradient algorithm (IVTCG), the IRW-$L_{1/2}$.

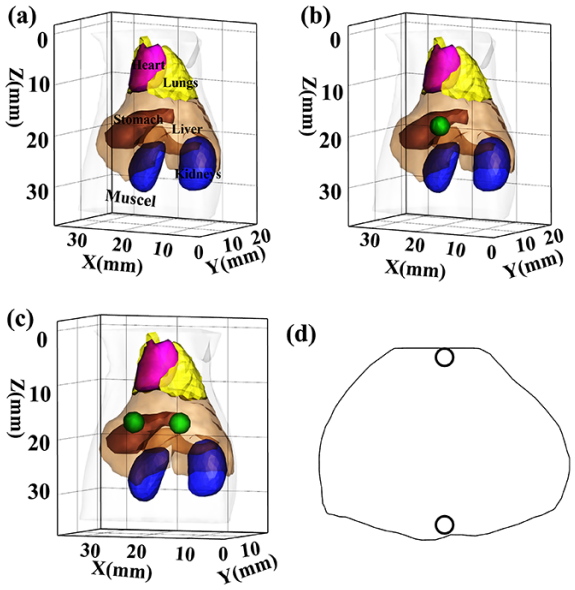

Fig. 1. (a) The 3D views of mouse model, (b) Torso of the mouse atlas model with one spherical fluorescent target in the stomach, (c) Torso of the mouse atlas model with two spherical fluorescent targets in the stomach, (d) Point excitation sources on the plane of Z = 17.5mm. The two circles denote the point excitation sources.

A. Single-target reconstruction on 3D digital mouse atlas

In the single-target experiment, the forward FEM mesh was discretized into 15847 nodes and 82847 tetrahedral elements. In the process inverse reconstruction, the FEM mesh was discretized into 10774 nodes and 55203 tetrahedral elements, and the central position of the true fluorescent target is (18, 6, 17.5) mm. Fig. 2(a)-(d) shows the cross-sectional and three-dimensional renderings of the four methods respectively. Table 3 presents the quantitative results of the four methods in single-target experiments. From fig 2 and Table 3 can get: FB and IRW-$L_{1/2}$. have higher CNR; FB has a smaller artifact and smaller error than the other three methods;

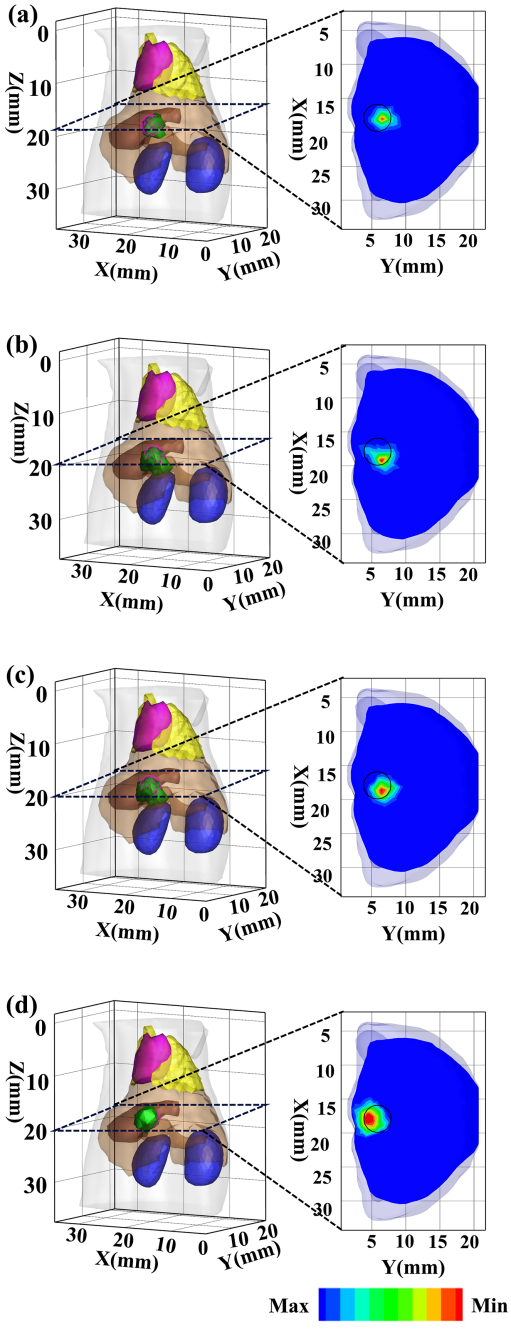

Fig. 2. Reconstruction results in the case of single target. Where (a) shows the reconstruction results of FBS, (b) shows the reconstruction results of DCA, (c) shows the reconstruction results of IVTCG, (d) shows the reconstruction results of IRW-$L_{1/2}$. (a) (d) shows 3D rendering the cross-section views of reconstructions by four comparative methods. In the 3D rendering red grid represent the real target and the green area represent the reconstruction target. The cross-section views of reconstructions by four comparative methods at the axial slice (z = 17.5mm) where the center of the real fluorescent target (denoted by the small black circle) is located.

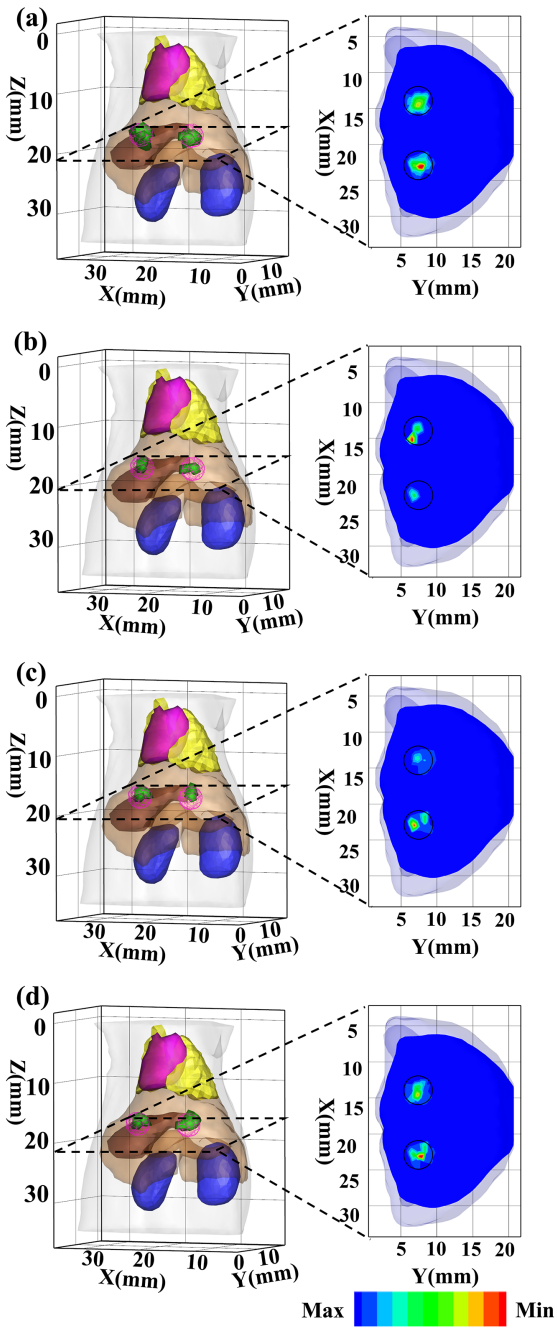

Fig. 3. Reconstruction results in the case of double target. Where (a) shows the reconstruction results of FB, (b) shows the reconstruction results of DCA, (c) shows the reconstruction results of IVTCG, (d) shows the reconstruction results of IRW-$L_{1/2}$. (a)-(d) shows 3D rendering the cross-section views of reconstructions by four comparative methods. In the 3D rendering red grid represent the real target and the green area represent the reconstruction target. The cross-section views of reconstructions by four comparative methods at the axial slice (z = 17.5mm) where the center of the real fluorescent target (denoted by the small black circle) is located.

At the same time, FB has the largest dice coefficient among the four methods, which indicates that the shape fitting of FB is also superior to other methods.

TABLE III
Quantitative results in single-target experiment

Method	Reconstruction source center(mm)	LE(mm)	DICE	CNR
FBS	(18.08, 6.62, 17.59)	0.54	0.67	53.16
DCA	(18.92, 6.17, 18.66)	1.49	0.40	21.90
IVTCG	(18.20, 6.70, 17.86)	1.02	0.51	30.53
IRW-$L_{1/2}$	(18.20, 5.94, 17.33)	0.71	0.60	59.08

B. Double-target reconstruction on 3D digital mouse atlas

In the double-target experiment, the forward FEM mesh was discretized into 12993 nodes and 67069 tetrahedral elements. In the process inverse reconstruction, the FEM mesh was discretized into 10774 nodes and 55203 tetrahedral elements. The central positions of the two true fluorescence targets are (23, 7.5, 17) and (14, 7.5, 17) mm, respectively Fig. 3(a)-(d) shows the cross-sectional and three-dimensional renderings of the four methods respectively. Table 4 presents the quantitative results of the four methods in double-target experiments. From fig 3, We can clearly see that the reconstruction result of FBS method is the best fit with the real light source, which is also proved by DICE in Table 4. And from Table 4, we can get: FBS has a smaller artifact and smaller error than the other three methods.

TABLE IV
Quantitative results in single-target experiment

Method	Reconstruction source center(mm)	LE(mm)	DICE	CNR
FBS	(23.09, 7.83, 16.70)	0.45	0.67	31.36
	(14.60, 7.36, 17.02)	0.61	0.43	
DCA	(23.03, 7.66, 16.35)	0.66	0.53	17.08
	(15.10, 6.49, 17.02)	1.51	0.44	
IVTCG	(23.03, 7.66, 16.35)	0.66	0.50	11.19
	(14.11, 7.84, 16.12)	0.84	0.22	
IRW-$L_{1/2}$	(21.85, 8.14, 16.68)	1.34	0.19	3.21
	(13.93, 7.03, 17.59)	0.73	0.33	

IV. DISCUSSION AND CONCLUSION

In this study, we proposed $L_1 - L_2$ norm regularization to overcome the ill-posedness of FMT reconstruction. By derived the proximal operator of $L_1 - L_2$ norm, we can use the framework of FBS method solve efficiently. We demonstrated the performance of proposed FBS method in FMT with simulated data on a heterogeneous mouse model. By through comparison experiment on single and double source reconstruction, we can get the proposed FBS method outperformed several typical reconstruction algorithms such as DCA, IVTCG, IRW-$L_{1/2}$.

Although FBS has achieved better results, the problems of FBS still have shortcomings that need to be resolved. It should be noted that our proposed method may not be suitable for all situations, because in the digital simulation experiment, the FBS method was only utilized to reconstruct the fluorescence targets in liver. Moreover, we are not performed in vivo experiments to verify the feasibility of the FBS method. It is also noted that in this work, we chose the regularization parameters according to experimental experience and our previous work on reconstruction, which is time consuming and unstable.

Thus, in the future study, we will carry out more experiments to verify the proposed method application and performance in the other tumor types or diseases. and we will focus on method development based on adaptive parameters. Future work will also focus on clinical research of FMT.

References

[1] M. Koch, P. Symvoulidis, and V. Ntziachristos, "Tackling standardization in fluorescence molecular imaging," Nature Photonics, vol. 12, no. 9, pp. 505–515, 2018.

[2] H. Guo, L. Gao, J. Yu, X. He, H. Wang, J. Zheng, and X. Yang, "Sparse-graph manifold learning method for bioluminescence tomography," Journal of biophotonics, vol. 13, no. 4, p. e201960218, 2020.

[3] A. Ale, V. Ermolayev, E. Herzog, C. Cohrs, M. H. De Angelis, and V. Ntziachristos, "Fmt-xct: in vivo animal studies with hybrid fluorescence molecular tomography–x-ray computed tomography," Nature methods, vol. 9, no. 6, pp. 615–620, 2012.

[4] X. He, H. Meng, X. He, K. Wang, X. Song, and J. Tian, "Nonconvex laplacian manifold joint method for morphological reconstruction of fluorescence molecular tomography," Molecular Imaging and Biology, pp. 1–13, 2021.

[5] Y. Liu, S. Jiang, J. Liu, Y. An, G. Zhang, Y. Gao, K. Wang, and J. Tian, "Reconstruction method for fluorescence molecular tomography based on l1-norm primal accelerated proximal gradient," Journal of biomedical optics, vol. 23, no. 8, p. 085002, 2018.

[6] H. Guo, X. He, M. Liu, Z. Zhang, Z. Hu, and J. Tian, "Weight multispectral reconstruction strategy for enhanced reconstruction accuracy and stability with cerenkov luminescence tomography," IEEE transactions on medical imaging, vol. 36, no. 6, pp. 1337–1346, 2017.

[7] H. Guo, J. Yu, Z. Hu, H. Yi, Y. Hou, and X. He, "A hybrid clustering algorithm for multiple-source resolving in bioluminescence tomography," Journal of biophotonics, vol. 11, no. 4, p. e201700056, 2018.

[8] H. Guo, J. Yu, X. He, Y. Hou, F. Dong, and S. Zhang, "Improved sparse reconstruction for fluorescence molecular tomography with l 1/2 regularization," Biomedical optics express, vol. 6, no. 5, pp. 1648–1664, 2015.

[9] S. Jiang, J. Liu, Y. An, Y. Gao, H. Meng, K. Wang, and J. Tian, "Fluorescence molecular tomography based on group sparsity priori for morphological reconstruction of glioma," IEEE Transactions on Biomedical Engineering, vol. 67, no. 5, pp. 1429–1437, 2019.

[10] X. He, F. Dong, J. Yu, H. Guo, and Y. Hou, "Reconstruction algorithm for fluorescence molecular tomography using sorted l-one penalized estimation," JOSA A, vol. 32, no. 11, pp. 1928–1935, 2015.

[11] P. Mohajerani, A. A. Eftekhar, J. Huang, and A. Adibi, "Optimal sparse solution for fluorescent diffuse optical tomography: theory and phantom experimental results," Applied Optics, vol. 46, no. 10, pp. 1679–1685, 2007.

[12] S. Jiang, J. Liu, G. Zhang, Y. An, H. Meng, Y. Gao, K. Wang, and J. Tian, "Reconstruction of fluorescence molecular tomography via a fused lasso method based on group sparsity prior," IEEE Transactions on Biomedical Engineering, vol. 66, no. 5, pp. 1361–1371, 2018.

[13] H. Guo, L. Gao, J. Yu, X. He, H. Wang, J. Zheng, and X. Yang, "Inside cover: Sparse-graph manifold learning method for bioluminescence tomography (j. biophotonics 4/2020)," Journal of Biophotonics, vol. 13, no. 4, p. e202070011, 2020.
[14] X. He, J. Liang, X. Wang, J. Yu, X. Qu, X. Wang, Y. Hou, D. Chen, F. Liu, and J. Tian, "Sparse reconstruction for quantitative bioluminescence tomography based on the incomplete variables truncated conjugate gradient method," Optics Express, vol. 18, no. 24, pp. 24 825–24 841, 2010.
[15] X. He, J. Yu, X. Wang, H. Yi, Y. Chen, X. Song, and X. He, "Half thresholding pursuit algorithm for fluorescence molecular tomography," IEEE Transactions on Biomedical Engineering, vol. 66, no. 5, pp. 1468–1476, 2018.
[16] H. Zhang, G. Geng, X. Wang, X. Qu, Y. Hou, and X. He, "Fast and robust reconstruction for fluorescence molecular tomography via regularization," BioMed research international, vol. 2016, 2016.
[17] B. Dogdas, D. Stout, A. F. Chatziioannou, and R. M. Leahy, "Digimouse: a 3d whole body mouse atlas from ct and cryosection data." Physics in Medicine Biology, vol. 52, no. 3, pp. 577–587, 2007.
[18] H. Guo, Y. Hou, X. He, J. Yu, J. Cheng, and X. Pu, "Adaptive hp finite element method for fluorescence molecular tomography with simplified spherical harmonics approximation," Journal of Innovative Optical Health Sciences, vol. 7, no. 02, p. 1350057, 2014.